

A General Approach to Binary and Ternary Hybrid Nanocrystals

Weili Shi,[†] Hao Zeng,^{*,‡} Yudhistira Sahoo,[§] Tymish Y. Ohulchansky,[§]
Yong Ding,^{||} Zhong Lin Wang,^{||} Mark Swihart,^{*,†} and Paras N. Prasad^{*,§}

Institute for Lasers, Photonics, and Biophotonics, Department of Chemical and Biological Engineering, Department of Physics, and Department of Chemistry, The University at Buffalo (SUNY), Buffalo, New York 14260, and School of Materials Science and Engineering, Georgia Institute of Technology, Atlanta, Georgia 30332

Received January 13, 2006; Revised Manuscript Received February 17, 2006

ABSTRACT

We describe and demonstrate a general strategy for engineering binary and ternary hybrid nanoparticles based on spontaneous epitaxial nucleation and growth of a second and third component onto seed nanoparticles in high-temperature organic solutions. Multifunctional hybrid nanoparticles that combine magnetic, plasmonic, and semiconducting properties and that are tunable in size and morphology can be realized, as demonstrated for combinations of Au, Fe₃O₄, and PbS or PbSe. The properties of each component within the hybrids can be modulated strongly by the conjugating component(s) aided by the coherent interfaces between them.

An important research direction in nanomaterials synthesis is the expansion from single-component nanoparticles to hybrid nanostructures with discrete domains of different materials arranged in a controlled fashion. Thus, different functionalities can be integrated, with the dimension and material parameters of the individual components optimized independently. It can even provide entirely novel properties via the coupling between components. Because many physical properties have fundamental length scales of a few to a few hundred nanometers, compositional control at such length scales provides tremendous possibilities for achieving new combinations of these properties. Progress in nanomaterial synthesis has made it possible to uniformly mix nanoscale components in hybrid materials.^{1,2} However, the random nucleation of a second phase¹ or the random mixing of different components,² provides limited control over the size and position of the components. Recently, by coassembling different nanoparticles with specific size ratios, precisely ordered three-dimensional binary superlattices have been created.^{3–5} Progress has also been made on the synthesis of symmetric core–shell hybrid nanoparticles,^{6–12} nonsymmetric dimers,^{13–17} and other heterostructures.^{18–20}

Here we report a straightforward technique for making nearly monodisperse binary and ternary hybrid nanoparticles

(NPs) with coherent, quasi-epitaxial interfaces made up of different classes of materials. Furthermore, we show that morphologies other than simple core–shell and dimer nanostructures can be produced rationally. Four classes of hybrid NPs are presented: magnetic–metallic (XFe₂O₄–Au, X = Fe, Mn, Co), semiconductor–metallic (PbS–Au, PbSe–Au), semiconductor–magnetic (PbS–Fe₃O₄), and three-component magnetic–metallic–semiconductor (Fe₃O₄–Au–PbS, Fe₃O₄–Au–PbSe) hybrid NPs. Morphologies include spherical and cubic core–shell, peanutlike, dumbbell-like, and more complex structures. These nanoparticles self-assemble into quasi-ordered structures, leading to quasi-periodic modulation of composition. The resulting hybrid materials not only retain their individual magnetic, semiconducting, and plasmonic properties but these properties are also appreciably affected by the conjugating component(s).

Magnetic–Metallic Hybrid Nanoparticles. Here we use Au–Fe₃O₄ hybrid nanoparticles as an example for magnetic–metallic hybrid nanoparticle synthesis, but we have also prepared similar Au–MnFe₂O₄ and Au–CoFe₂O₄ nanoparticles. Au nanoparticles were synthesized using the Brust two-phase method.²¹ Hybrid nanoparticles were prepared by decomposition of iron acetylacetonate (Fe(acac)₃) on the surfaces of Au nanoparticles in high-boiling-point solvents in the presence of oleic acid and oleylamine, as described in greater detail in the Supporting Information. A two-stage heating strategy was used, first holding the mixture at 205 °C for 2 h, then heating to reflux (~300 °C). Different morphologies were obtained by varying the solvent, precursor ratios, and heating rates, with the most convenient control

* Corresponding authors. E-mail: haozeng@buffalo.edu; swihart@eng.buffalo.edu; pnprasad@buffalo.edu.

[†] Institute for Lasers, Photonics, and Biophotonics and Department of Chemical and Biological Engineering, The University at Buffalo.

[‡] Department of Physics, The University at Buffalo.

[§] Institute for Lasers, Photonics, and Biophotonics and Department of Chemistry, The University at Buffalo.

^{||} Georgia Institute of Technology.

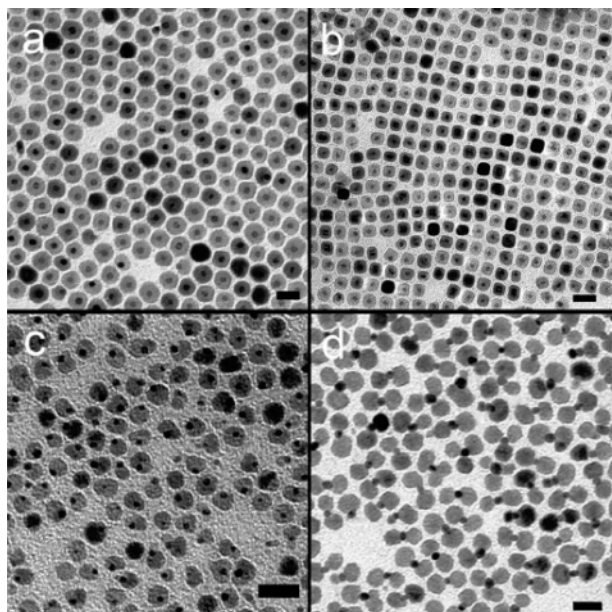


Figure 1. TEM images of spherical (a), cubic (b), peanutlike (c), and dumbbell-like (d) Au–Fe₃O₄ hybrid nanoparticles. The scale bars are 20 nm.

of morphology provided by the choice of solvent. For example, octyl ether produced peanutlike particles, benzyl ether and phenyl ether gave core–shell particles, and octadecene yielded a mixture of peanutlike and core–shell structures. Peanutlike nanoparticles were also prepared from iron carbonyl (Fe(CO)₅), as described previously by Yu et al.¹⁴ Although Fe(CO)₅ did not yield the other morphologies shown here, it provided the fastest synthesis of peanutlike particles, and peanutlike particles from Fe(acac)₃ or from Fe(CO)₅ could be used interchangeably, with similar results in subsequent preparation of dumbbell-like and ternary hybrid nanoparticles.

Figure 1 shows typical TEM images of Au–Fe₃O₄ hybrid nanoparticles. The individual components are nearly monodisperse, and therefore the hybrid nanoparticles exhibit narrow size and shape distributions and often self-assemble into ordered arrays. Four different morphologies are shown: spherical core–shell, spherical core-cubic shell, peanutlike particles with a smaller gold nanoparticle partially embedded in a larger Fe₃O₄ nanoparticle, and dumbbell-like particles with two Fe₃O₄ nanoparticles connected by a Au nanoparticle. High-resolution TEM (HRTEM) images (Figure 2) show that both components are single-crystalline and the interfaces between them are coherent. HRTEM images consistently showed parallel lattice planes for Au and Fe₃O₄, with lattice spacings of 2.36 and 4.86 Å, respectively, which correspond to the {111} lattice planes in both materials. As a result of the small lattice mismatch (~3%) between 2d₁₁₁(Au) and d₁₁₁(Fe₃O₄), the Fe₃O₄ grows epitaxially on the Au nanoparticles. Electron diffraction patterns from these structures (Figure 2b,d) show ring patterns from the face-centered cubic and cubic spinel structures of Au and Fe₃O₄, respectively. The Au diffraction rings are much weaker because of the small volume fraction of gold. For the nanoparticles with cubic Fe₃O₄ shells, the electron diffraction shows enhanced {400} and {440} reflections from Fe₃O₄ (Figure

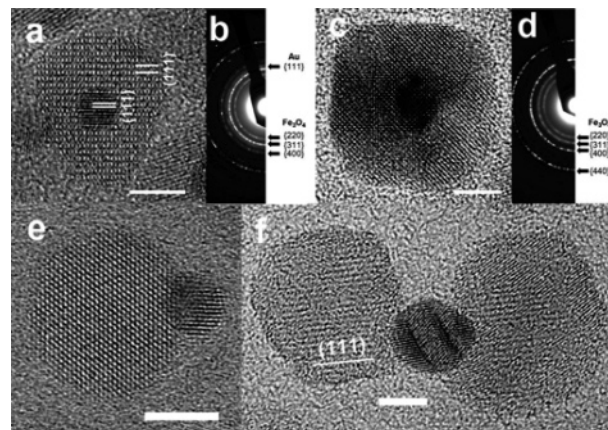


Figure 2. HRTEM images and electron diffraction patterns from spherical (a and b), cubic (c and d), peanutlike (e), and dumbbell-like (f) hybrid nanoparticles. The scale bars are 4 nm.

2d). HRTEM images (Figure 2c) show {440} lattice fringes in the face diagonals and {100} planes parallel to the cubic edges of Fe₃O₄ shells, suggesting that the terminating facets are {100} planes. Alignment of the <100> axis perpendicular to the substrate enhances the intensity of both the {100} and {110} reflections.

Under the conditions used here, Fe₃O₄ invariably forms on the gold nanoparticles, but using a smaller amount of gold seeds leads to a mixture of free Fe₃O₄ nanoparticles and core–shell structures. Thus, Fe₃O₄ nucleates preferentially on the gold seeds, rather than homogeneously. The final morphology depends on whether the Au surface allows only a single nucleation site or multiple ones. As suggested by Yu et al., upon nucleation of Fe₃O₄ on the Au surface, electron density from the Au nanoparticle is drawn to the polar Au/Fe₃O₄ interface.¹⁴ Free electrons in the gold nanoparticle may also catalyze the Fe₃O₄ nucleation. Solvents such as benzyl ether and phenyl ether contain aromatic rings, which are good electron donors. Their coordination to the Au particles may replenish the electronic deficiency on the latter, consequently allowing additional nuclei to form on the Au surface, which can grow and eventually coalesce to form core–shell structures. To investigate this, we stopped the reaction after heating at 205 °C for 30 min in phenyl ether or benzyl ether. This yielded flowerlike particles with several Fe₃O₄ “petals” surrounding the Au core (see Supporting Information, Figure S1). At this relatively low temperature and short time, the “petals” had not yet fused into a continuous shell. In contrast, solvents with largely saturated hydrocarbon chains such as octyl ether and octadecene are not effective electron donors, and it may be that once a single Fe₃O₄ nucleus is present further nucleation is not possible without electron donation from the solvent. Further growth of Fe₃O₄ from a single site forms a peanutlike particle. In the case of octadecene, where there is only one π bond per molecule, with electron donating ability between that of octyl ether and benzyl/phenyl ether, there may be only a partial replenishment of electrons on Au, resulting in a mixture of core–shell and peanutlike structures. The nanoparticle shape depends on the growth rate along different crystal axes. When all growth rates are roughly equal, quasi-spherical particles (typically truncated octahedra or cuboc-

tahedra) will form, as observed when the solvent was benzyl ether. However, if one crystal face grows substantially faster than the others, then it will grow itself out of existence, leaving behind slower-growing faces. Thus, in phenyl ether, the growth rate along the $\langle 111 \rangle$ direction exceeded that along the $\langle 100 \rangle$ direction, yielding cubic nanoparticles with exposed $\{100\}$ faces; thus, it appears that phenyl ether promotes $\langle 111 \rangle$ growth or suppresses $\langle 100 \rangle$ growth.

Dumbbell-like particles were prepared by heating peanutlike particles in the presence of sulfur. They consist of two 10 nm spherical Fe_3O_4 nanoparticles connected by a ~ 3.8 nm Au particle (Figure 1d), formed by fusing of the Au ends of two peanutlike nanoparticles. Simply heating peanutlike particles did not yield dumbbell-like particles. The addition of sulfur is critical to dumbbell formation: it bonds Au strongly and appears to aid in the sintering of gold particles.

Keeping the reaction mixture at 205 °C for 2 h, before heating to reflux, is critical for forming monodisperse hybrid particles. The Fe_3O_4 precursor, $\text{Fe}(\text{acac})_3$, has a decomposition temperature around 190 °C. At temperatures slightly above this, heterogeneous nucleation on the gold nanoparticles dominates and growth of these nuclei is slow because of the low concentration of free metal ions. Significant growth occurs only at more elevated temperatures, in this case the reflux temperatures, near 300 °C. Thus, the nucleation and growth is separated temporally. When the mixture is heated rapidly to reflux, the size distribution is much broader because of simultaneous nucleation and growth. Similar results were observed for Fe_3O_4 nanoparticles by Sun and Zeng.²²

Semiconductor–Metallic Hybrid Nanoparticles. Both Au–PbS and Au–PbSe hybrid particles were prepared by adapting the synthesis procedure for the neat semiconductor particles. Au nanoparticles were mixed with a Pb-oleate complex (formed by reacting PbO and oleic acid), then a sulfur or selenium solution was added, followed by heating under airless conditions, as described in greater detail in the Supporting Information. Figure 3 shows semiconductor–metal hybrid particles with different morphologies. The diameters of the Au part for the peanutlike structures are 3 nm (Figure 3a) and 5 nm (Figure 3b); while those of the PbS part are 6 nm (Figure 3a) and 8 nm (Figure 3b). In the sample shown in Figure 3c, about 95% of the particles have dumbbell-like structures with two PbS arms connected by Au, and the other 5% of particles are tripods with Au connecting three PbS arms. The average Au diameter in dumbbell-like (tripod) particles is about 3.8 nm (4.3 nm), equivalent in volume to two (three) 3 nm Au nanoparticles. The Au–PbSe hybrid nanoparticles had a core–shell morphology with 2 nm Au cores and 1.5 nm PbSe shells (Figure 3d). The electron diffraction patterns of both Au–PbS (Figure 4c) and Au–PbSe (Figure 4d) show the face-centered cubic structure of Au and the cubic rock-salt structure of PbS or PbSe, with the expected lattice spacings. High-resolution TEM (Figure 4a, b, e, f, and g) reveals that the Au and PbS(Se) are single-crystalline and there are coherent interfaces between them in all hybrid structures.

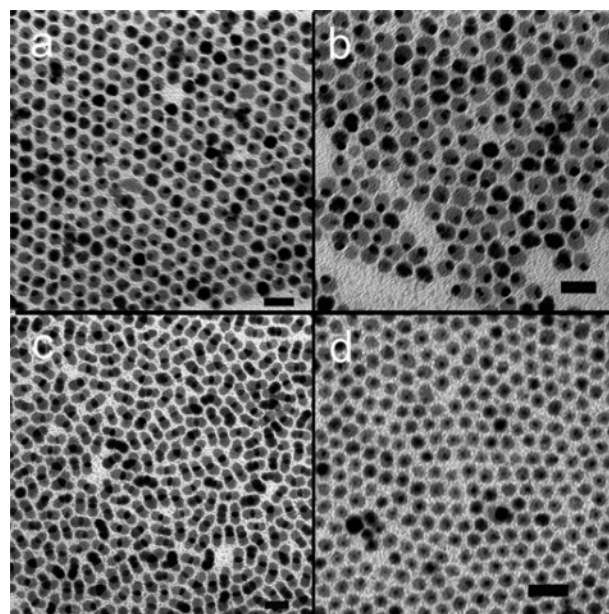


Figure 3. TEM images of 3 nm Au–6 nm PbS peanutlike (a), 5 nm Au–8 nm PbS peanutlike (b), Au–PbS dumbbell-like (c), and Au–PbSe core–shell (d) hybrid nanoparticles. The scale bars are 20 nm.

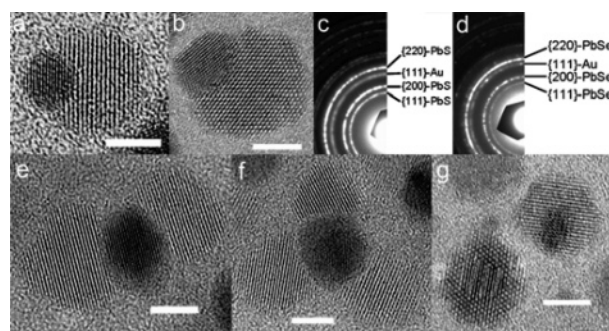


Figure 4. HRTEM images of 3 nm Au–6 nm PbS (a), 5 nm Au–8 nm PbS (b), Au–PbS dumbbell (e) Au–PbS tripod (f), and Au–PbSe core–shell (g) hybrid nanoparticles. Typical electron diffraction patterns from Au–PbS (c) and Au–PbSe (d) structures. The scale bars are 4 nm.

The mechanisms of formation of Au–PbS and Au–PbSe may be broadly similar to that of Au– Fe_3O_4 . However, the epitaxial relationship in these cases is less obvious. For Au–PbS, the predominant relative orientation of the Au and PbS lattices is as shown in Figure 4a and e in which the Au(111) planes are parallel to the PbS(200) planes and parallel to the interface between the particles. This implies that the interface is between a (111) face of Au and a (100) face of PbS. Perpendicular to these faces are the (110) planes of Au and the (100) planes of PbS. The difference in lattice spacing between these is only 3%, but the Au(110) planes are arranged with hexagonal symmetry, while the PbS(100) planes have square symmetry. The registration between these two lattices is illustrated in Figure S2 in the Supporting Information.

During synthesis of these Au–PbS hybrid nanoparticles, once sulfur is injected into the reaction flask containing the Pb-oleate complex and Au nanoparticles, there may be a

competition between the adsorption of sulfur onto the Au surface and reaction with the Pb-oleate to form PbS nanoparticles. The combination of these leads to heterogeneous nucleation of PbS on the surface of the Au. The morphology of Au–PbS hybrid nanoparticles is controlled primarily by the Au/precursor ratio and the growth temperature. In all reactions, we fixed the PbO:S ratio at 3:1 while varying the Au seed concentration. When the ratio of Au to sulfur is high (1:10), the nucleation of PbS on the Au surface depletes all of the sulfur rapidly, and hence only peanutlike particles are formed. When a lower Au to sulfur ratio (1:20) is used, excess sulfur remains present long enough to link two or three Au particles together and catalyze their fusion into a single nanocrystal, similar to the sulfur-catalyzed fusion observed for the Au–Fe₃O₄ nanoparticles. Each of these component particles already has a PbS nucleus growing on it, and these can then continue to grow on opposite sides of the fused Au particle to form a dumbbell-like structure, as shown in Figures 3c and 4e. In the case of PbSe, TOP–Se is injected into the hot reaction mixture containing free Au nanoparticles and Pb-oleate complex and the reaction is quenched after 1 min., as in procedures used to prepare monodispersed PbSe nanocrystals. Rapid simultaneous nucleation, epitaxial growth, and fusing of multiple nuclei may lead to the formation of the core–shell structures observed, but even in this very rapid reaction heterogeneous nucleation dominates homogeneous nucleation and free PbSe nanocrystals do not form.

A key difference between the Au–PbS preparation and the Au–Fe₃O₄ preparation was that changes in solvent did not affect the morphology of the Au–PbS hybrid particles as they did for the Au–Fe₃O₄. For a given seed particle concentration, the same morphology was obtained using trioctylamine, phenyl ether, or octadecene as the solvent. This observation makes clear that while the overall approach of solution-phase heteroepitaxy used here can be quite general, the solvent, surfactant, and reaction temperature must be tailored for each individual material, and effects such as morphology control that are attainable for one material may not be possible for others. In each case, one can start from solvent, surfactant, and temperature combinations used for synthesis of single component particles of the phase to be grown, as we did in this case, starting from conditions known to produce high-quality PbS particles. Ideally, heterogeneous nucleation on the seed particles will dominate homogeneous nucleation at these conditions or at slightly milder ones where the driving force for growth of the new phase is somewhat smaller, and hybrid nanoparticles will be obtained.

Magnetic–Semiconductor Hybrid Nanoparticles. PbS–Fe₃O₄ hybrid nanoparticles were synthesized by the same method as Au–Fe₃O₄ hybrid nanoparticles but using PbS nanoparticles as seeds. The reaction temperature was increased directly to reflux quickly, without holding at 200 °C, to avoid aggregation and sintering of PbS that occurs at that temperature. Once a thin shell of Fe₃O₄ formed on the PbS seeds, the aggregation was prevented. TEM and HRTEM images of the resulting core–shell PbS–Fe₃O₄ hybrid nanoparticles with 8 nm single-crystal PbSe cores and 4 nm

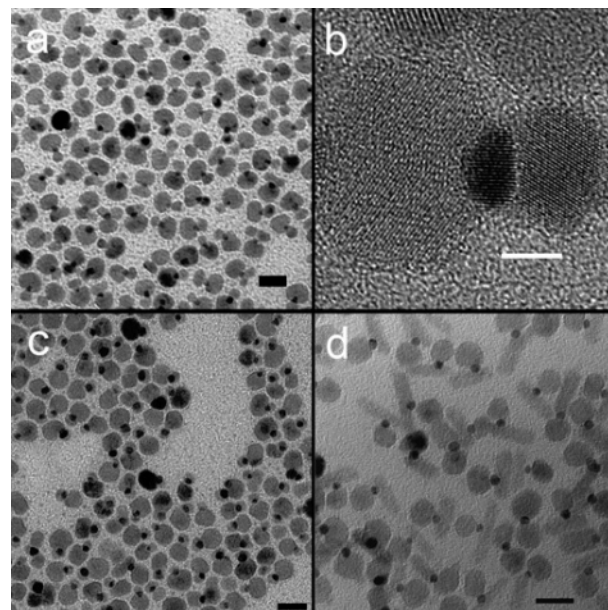


Figure 5. TEM images (a, c, and d) and HRTEM image (b) of Fe₃O₄–Au–PbSe (a and b) and Fe₃O₄–Au–PbS (c and d) ternary hybrid nanoparticles. The scale bars are 20 nm in a, c, and d and 4 nm in b.

polycrystalline Fe₃O₄ shells are shown in the Supporting Information (Figure S3). Electron diffraction patterns show the rock salt and the cubic spinel structures of PbS and Fe₃O₄, respectively. Such a synthesis of PbSe/Fe₃O₄ hybrids was not possible because of the greater propensity of PbSe nanoparticles to agglomerate and sinter at these temperatures. The synthesis in the reverse order (PbS or PbSe on Fe₃O₄ seeds) did not lead to nucleation of PbS or PbSe on the Fe₃O₄, perhaps because of the lack of surface reactivity of Fe₃O₄ at the relatively low temperatures used for PbS and PbSe synthesis.

Magnetic–Metallic–Semiconductor Ternary Hybrid Nanoparticles. Fe₃O₄–Au–PbSe ternary hybrid nanoparticles were prepared using Au–Fe₃O₄ peanutlike nanoparticles with 12 nm Fe₃O₄ and 3–4 nm Au components as seeds. As shown in Figure 5a, more than 80% of the PbSe components are dotlike, about 5 nm in diameter, and the remainder are rodlike, with typical dimensions of 10 nm by 3 nm. As the Au-to-PbO ratio was lowered, the PbSe part transformed from spherical to rodlike. This is understandable in the context of a mechanism where the Au seed promotes anisotropic growth, which proceeds to a greater extent at higher precursor concentration. HRTEM (Figure 5b) again shows coherent interfaces between the components, and the electron diffraction pattern is as expected (see Supporting Information, Figure S4). The same Au–Fe₃O₄ peanutlike hybrid nanoparticles were used as seeds to prepare Fe₃O₄–Au–PbS ternary hybrid nanoparticles. Figure 5 shows TEM images of Fe₃O₄–Au–PbS ternary hybrid nanoparticles in which the PbS parts are spherical, about 2 nm in size (Figure 5c), or rodlike, with average dimensions of about 7 nm by 25 nm (Figure 5d). Once again, electron diffraction showed the expected crystalline structures, but it was difficult to

resolve lattice fringes for the PbS component in HRTEM for rod-shaped PbS (see Supporting Information, Figure S5).

The heating strategy and seed particle dimensions were important for forming ternary hybrids. If the gold component was less than 3 nm in diameter, then nucleation of PbS or PbSe was difficult, presumably because of the small amount of gold surface area exposed. For Fe₃O₄-Au-PbS, if the temperature of the reaction mixture was quickly increased to 150 °C after sulfur injection, both dumbbell-like Au-Fe₃O₄ hybrid nanoparticles (as in Figure 1d) and Fe₃O₄-Au-PbS ternary hybrid nanoparticles (as in Figure 5d) were formed. This suggests that some Au-Fe₃O₄ peanutlike particles aggregated to form dumbbell-like Au-Fe₃O₄ particles in the presence of sulfur before PbS could nucleate and grow on Au-Fe₃O₄. When the temperature was held at 100 °C after sulfur injection, Fe₃O₄-Au-PbS (dot shaped, as in Figure 5c) formed and no dumbbell-like Au-Fe₃O₄ particles were observed.

A clear difference between the binary Au-PbS or Au-PbSe particles compared to the corresponding ternary Fe₃O₄-Au-PbS or Fe₃O₄-Au-PbSe particles was the propensity for rodlike growth of the semiconductor component in the ternary structures, which was not observed in the binary structures. Under the conditions used here, rodlike growth does not occur on the metal particles alone. However, in a separate study,²³ we have shown that PbSe rods can be grown from pure noble metal seed particles under similar conditions, but using a ratio of seed particles to precursor molecules that is about a factor of 50 lower than that used here. It appears that the binary seed particles used to form ternary hybrid particles promote rodlike growth of the semiconductor component by limiting the amount of metal surface exposed for growth. Seeded anisotropic growth of nanocrystals in solution is often attributed to the solution-liquid-solid (SLS) mechanism first proposed by Trentler et al.²⁴ However, in the present case, it is extremely unlikely that the metallic component of the binary seed particle becomes molten, even accounting for size-dependent melting point depression and the possibility of Au-Pb intermetallic compounds. So, we propose that the role of the gold is simply to provide a low-energy surface for the initial nucleation of the PbS or PbSe phase.

Optical Properties. Au nanoparticles exhibit strong surface plasmon resonance (SPR) absorption. Both Au-Fe₃O₄ and Au-PbS hybrid nanoparticles also exhibit SPR, but the resonance frequencies are red shifted. To study this, we used Au-Fe₃O₄ core-shell nanoparticles with 10 nm cores because much smaller Au nanoparticles (3 nm) show little or no SPR²⁵ absorption. As shown in Figure 6a, 10 nm Au NPs have a SPR peak centered at 520 nm, consistent with previous studies.²⁶ As the Au core is coated with Fe₃O₄, the peak position shifts to 546 (partial shell), 559 (2 nm shell), and 573 nm (3 nm shell). Coating metal particles with a dielectric shifts the SPR frequency,²⁷ and because it has a high refractive index (~2.4), the effect of Fe₃O₄ on the SPR is large. For a given core-shell geometry, the extinction efficiency can be calculated quantitatively from Mie theory.²⁸ We have simulated the absorption spectrum using the

equations presented by Toon and Ackerman,²⁹ the frequency-dependent complex refractive index of gold, and a frequency-independent refractive index of 2.42 for Fe₃O₄. Figure 6b shows that the shift in the SPR peak is well reproduced and that this dielectric coating effect can fully account for it. The charge state of the Au can also affect the SPR, and electron deficiency will shift the absorption to longer wavelength.²⁵ However, the resonance frequency is proportional to $N^{1/2}$, where N is the number of free electrons, so a 10% red shift from 520 to 573 nm would require a 20% decrease in the number of free electrons, which is not a very realistic scenario. Figure 6c shows the absorption spectra from Au-PbS hybrid nanoparticles, which exhibit similar red-shifts of the SPR frequency compared to pure gold nanoparticles. This can probably also be accounted for by dielectric effects, though a quantitative comparison is not simple for these asymmetric structures. The real part of the refractive index of PbS is about 4.3 at wavelengths of 500 to 600 nm, so the dielectric effects could be even larger for it than for Fe₃O₄.

PbS has a band gap of 0.41 eV and a Bohr exciton radius of ~20 nm. As a result, PbS nanocrystals display strong quantum confinement, with the absorption edge tunable from 0.41 to 2.32 eV.^{30,31} The absorption spectra in Figure 6c do not show an absorption peak in the infrared for pure PbS nanoparticles or Au-PbS hybrid nanoparticles, probably because of size polydispersity (~10%). However, the pure 8 nm PbS nanoparticles show intense photoluminescence (PL) at around 1750 nm (Figure 6d). For peanutlike hybrid NPs with PbS and Au parts of similar size (8 and 5 nm), the PL intensity was reduced by about a factor of 30 compared to the pure PbS nanoparticles (Figure 6d), and similar PL quenching was observed for other hybrid Au-PbS and Au-PbSe nanoparticles of different sizes and shapes (not shown). This cannot be accounted for simply by Au absorption of the excitation light because the quenching was similar at excitation wavelengths near (514 nm) and away from (840 nm) the Au SPR absorption. Further, the PL intensity ratio of quenched and normal emission for the two excitation wavelengths remains approximately the same, indicating that any PL loss due to absorption of excitation flux by Au is insignificant. We propose that PL is severely quenched because of the intimate contact of PbS with Au, which promotes charge separation by allowing electrons to transfer to Au.

Magnetic Properties. Interactions between components of these nanoparticles are manifested in their magnetic properties as well as in their optical properties. Hysteresis loops of 10 nm Fe₃O₄ and 10 nm Au/Fe₃O₄ NPs with a 3 nm Au core measured at 10 K are shown in Figure 7. The saturation field increases from 1 kOe for pure Fe₃O₄ nanoparticles to 10 kOe for Au/Fe₃O₄ hybrid nanoparticles. The coercivity (H_c) also increases from 200 to 800 Oe. The remanence ratio (S) for pure Fe₃O₄ is about 0.8, a typical value for a randomly oriented NP assembly with cubic anisotropy. But for the Au/Fe₃O₄ hybrid nanoparticles, S decreases to 0.5, a value expected for a randomly oriented array with a uniaxial anisotropy. This behavior cannot be accounted for by the less than 3% difference in the magnetic

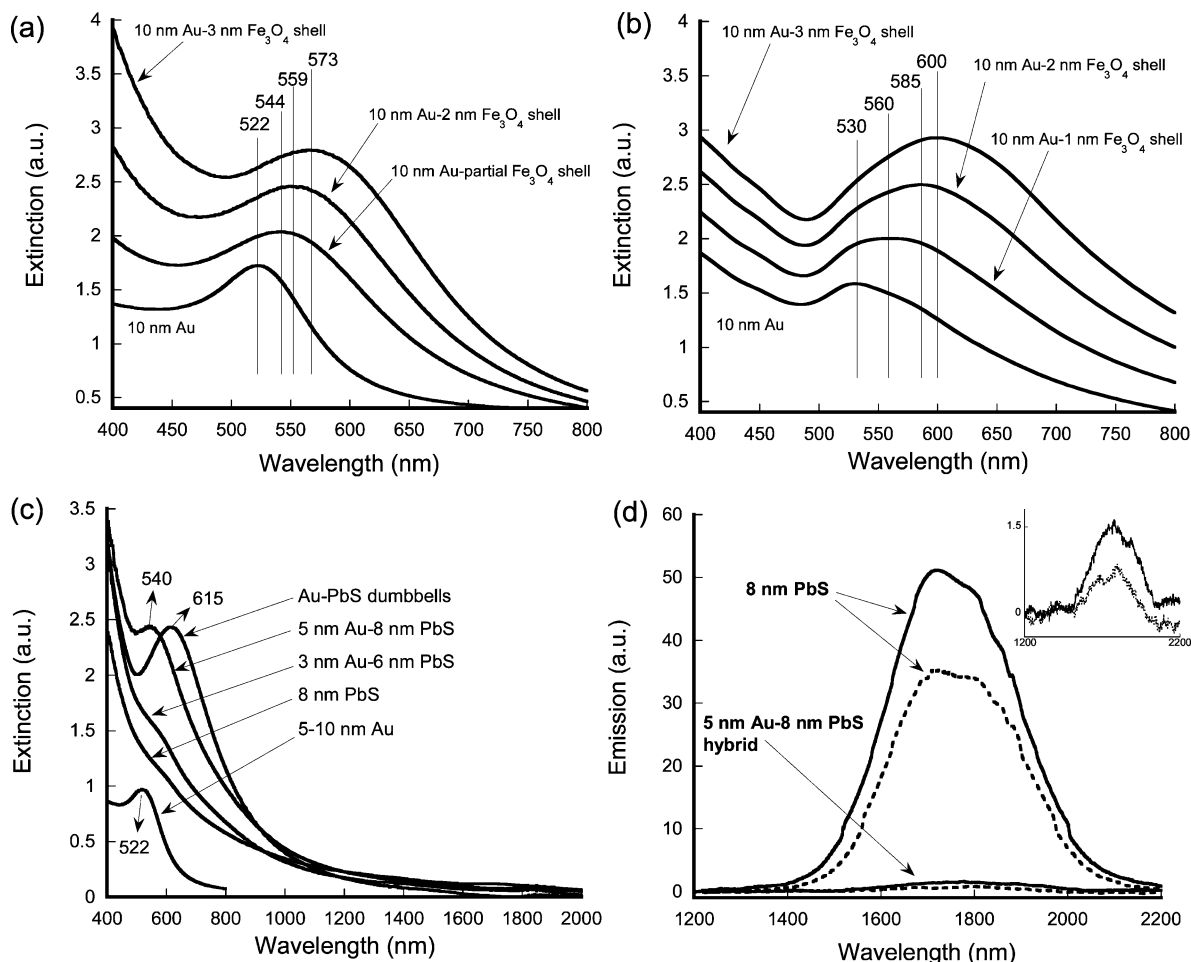


Figure 6. Optical response of hybrid nanoparticles. Measured absorbance spectra of Au–Fe₃O₄ (a), computed absorbance spectra of Au–Fe₃O₄ (b), measured absorbance spectra of Au–PbS hybrid nanoparticles (c), and photoluminescence emission spectra for PbS and Au–PbS hybrid nanoparticles (d). The effect of the conjugating component on the surface plasmon resonance of the gold can be observed (a–c). Quenching of photoluminescence occurs in the hybrid nanoparticles, compared to pure PbS nanoparticles (d). In d, the emission data are shown as solid curves for 514 nm excitation, and dashed curves for 840 nm excitation, while the inset shows the data for the hybrid nanoparticles on an expanded vertical scale.

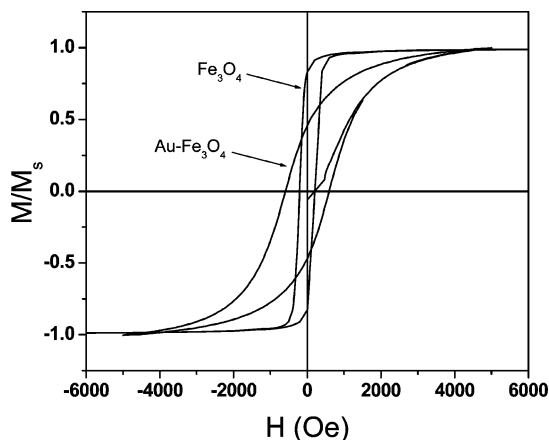


Figure 7. Magnetization hysteresis loops measured at 10 K, for assemblies of 10 nm Fe₃O₄ nanoparticles and spherical Au–Fe₃O₄ core–shell hybrid nanoparticles with 3 nm Au cores and 10 nm total diameter.

volume, but must be explained by a new anisotropy induced by the core–shell structure. This feature originates from the surface anisotropy: Fe atoms at the Au/Fe₃O₄ interface have

a reduced number of nearest neighbors, which decreases the interatomic exchange coupling. Thus, spins at the interface become canted and saturate only under very high fields. This provides an effective uniaxial anisotropy much like the surface anisotropy in nanoparticles and thin films, which dominates the original cubic anisotropy. The MnFe₂O₄–Au core–shell nanoparticles show similar effects, with even greater enhancement in coercivity, which increases from 140 Oe for MnFe₂O₄ to 880 Oe for Au–MnFe₂O₄ (see Supporting Information, Figure S6). This nonmagnetic core–magnetic shell approach can be viewed as a template-mediated synthesis technique for a magnetic nanoshell where the hollow shell can provide new spin structures different from solid spherical NPs. In a solid spherical NP of such a small size, the strong exchange coupling ensures that all of the spins will be aligned parallel to each other, both in their static configuration and during the dynamic magnetization reversal. For a hollow shell, however, the exchange coupling is significantly weaker, and the spins will not be able to keep aligned parallel to each other but rather their orientations will depend on the surface shape in order to minimize the

magnetostatic energy. The conventional “single-domain particle” picture is therefore no longer valid in such structures, even if their sizes are much smaller than the critical single-domain size. This would lead to interesting new magnetization reversal mechanisms that warrant further detailed studies. This simple example demonstrates the unique magnetic properties that can be realized with hybrid approaches.

In conclusion, we have demonstrated a versatile approach for preparing binary and ternary hybrid nanoparticles with different material combinations. The properties of each component can be strongly modulated by the other conjugating one(s). Self-assembling of these nanoparticles into thin films and bulk materials could lead to hybrid materials with tremendous design freedom, geometric complexity, and multifunctionality.

Acknowledgment. This work was supported in part by a Defense University Research Initiative on Nanotechnology grant, through the Chemistry and Life Sciences Directorate of the Air Force Office of Scientific Research.

Supporting Information Available: A more detailed description of the materials and methods used in synthesis and characterization; TEM image of “flowerlike” Au–Fe₃O₄ nanoparticles (Figure S1); schematic illustration of epitaxial relationship between Au and PbS (Figure S2); TEM, HR-TEM, and electron diffraction pattern for PbS–Fe₃O₄ core–shell nanoparticles (Figure S3); electron diffraction pattern for Fe₃O₄–Au–PbSe ternary hybrid nanoparticles (Figure S4); HRTEM and electron diffraction patterns for Fe₃O₄–Au–PbS ternary hybrid nanoparticles (Figure S5); and magnetization hysteresis loops for MnFe₂O₄ nanoparticles and spherical Au–MnFe₂O₄ core–shell hybrid nanoparticles (Figure S6). This material is available free of charge via the Internet at <http://pubs.acs.org>.

References

- Zheng, H.; Wang, J.; Lofland, S. E.; Ma, Z.; Mohaddes-Ardabili, L.; Zhao, T.; Salamanca-Riba, L.; Shinde, S. R.; Ogale, S. B.; Bai, F.; Viehland, D.; Jia, Y.; Schlom, D. G.; Wuttig, M.; Roytburd, A.; Ramesh, R. *Science* **2004**, *303*, 661–663.
- Zeng, H.; Li, J.; Liu, J. P.; Wang, Z. L.; Sun, S. H. *Nature* **2002**, *420*, 395–398.
- Redl, F. X.; Cho, K. S.; Murray, C. B.; O’Brien, S. *Nature* **2003**, *423*, 968–971.
- Shevchenko, E. V.; Talapin, D. V.; O’Brien, S.; Murray, C. B. *J. Am. Chem. Soc.* **2005**, *127*, 8741–8747.
- Shevchenko, E. V.; Talapin, D. V.; Kotov, N. A.; O’Brien, S.; Murray, C. B. *Nature* **2006**, *439*, 55–59.
- Zeng, H.; Li, J.; Wang, Z. L.; Liu, J. P.; Sun, S. H. *Nano Lett.* **2004**, *4*, 187–190.
- Kim, H.; Achermann, M.; Balet, L. P.; Hollingsworth, J. A.; Klimov, V. I. *J. Am. Chem. Soc.* **2005**, *127*, 544–546.
- Zeng, H.; Sun, S. H.; Li, J.; Wang, Z. L.; Liu, J. P. *Appl. Phys. Lett.* **2004**, *85*, 792–794.
- Skumryev, V.; Stoyanov, S.; Zhang, Y.; Hadjipanayis, G.; Givord, D.; Nogues, J. *Nature* **2003**, *423*, 850–853.
- Oldenburg, S. J.; Averitt, R. D.; Westcott, S. L.; Halas, N. J. *Chem. Phys. Lett.* **1998**, *288*, 243–247.
- Shi, W. L.; Sahoo, Y.; Swihart, M. T.; Prasad, P. N. *Langmuir* **2005**, *21*, 1610–1617.
- Kortan, A. R.; Hull, R.; Opila, R. L.; Bawendi, M. G.; Steigerwald, M. L.; Carroll, P. J.; Brus, L. E. *J. Am. Chem. Soc.* **1990**, *112*, 1327–1332.
- Gu, H. W.; Zheng, R. K.; Zhang, X. X.; Xu, B. *J. Am. Chem. Soc.* **2004**, *126*, 5664–5665.
- Yu, H.; Chen, M.; Rice, P. M.; Wang, S. X.; White, R. L.; Sun, S. H. *Nano Lett.* **2005**, *5*, 379–382.
- Kwon, K. W.; Shim, M. *J. Am. Chem. Soc.* **2005**, *127*, 10269–10275.
- Gu, H. W.; Yang, Z. M.; Gao, J. H.; Chang, C. K.; Xu, B. *J. Am. Chem. Soc.* **2005**, *127*, 34–35.
- Li, Y.; Zhang, Q.; Nurmikko, A. V.; Sun, S. *Nano Lett.* **2005**, *5*, 1689–1692.
- Kudera, S.; Carbone, L.; Casula, M. F.; Cingolani, R.; Falqui, A.; Snoeck, E.; Parak, W. J.; Manna, L. *Nano Lett.* **2005**, *5*, 445–449.
- Mokari, T.; Rothenberg, E.; Popov, I.; Costi, R.; Banin, U. *Science* **2004**, *304*, 1787–1790.
- Mokari, T.; Szturm, C. G.; Salant, A.; Rabani, E.; Banin, U. *Nat. Mater.* **2005**, *4*, 855–863.
- Brust, M.; Walker, M.; Bethell, D.; Schiffrin, D. J.; Whyman, R. *Chem. Commun.* **1994**, 801–802.
- Sun, S. H.; Zeng, H.; Robinson, D. B.; Raoux, S.; Rice, P. M.; Wang, S. X.; Li, G. X. *J. Am. Chem. Soc.* **2004**, *126*, 273–279.
- Yong, K.-T.; Sahoo, Y.; Chaudhury, K. R.; Swihart, M. T.; Minter, J. R.; Prasad, P. N. *Nano Lett.*, in press, 2006.
- Trentler, T. J.; Hickman, K. M.; Goel, S. C.; Viano, A. M.; Gibbons, P. C.; Buhro, W. E. *Science* **1995**, *270*, 1791–1794.
- Daniel, M. C.; Astruc, D. *Chem. Rev.* **2004**, *104*, 293–346.
- Brown, K. R.; Walter, D. G.; Natan, M. J. *Chem. Mater.* **2000**, *12*, 306–313.
- LizMarzan, L. M.; Giersig, M.; Mulvaney, P. *Langmuir* **1996**, *12*, 4329–4335.
- Aden, A. L.; Kerker, M. *J. Appl. Phys.* **1951**, *22*, 1242–1246.
- Toon, O. B.; Ackerman, T. P. *Appl. Opt.* **1981**, *20*, 3657–3660.
- Chen, S. W.; Truax, L. A.; Sommers, J. M. *Chem. Mater.* **2000**, *12*, 3864–3870.
- Wise, F. W. *Acc. Chem. Res.* **2000**, *33*, 773–780.

NL0600833

The American robin.



HIGHLIGHTS OF THE RECENT LITERATURE

EPIDEMIOLOGY

Seasonal Tastes

The mosquito-borne West Nile virus (WNV) has caused repeated human epidemics in North America and is a zoonotic virus transmitted by *Culex* mosquitoes whose preferred host is the emblematic American robin (*Turdus migratorius*). Kilpatrick *et al.* have shown that the mosquitoes exhibit a shift in feeding behavior when the robins disperse after breeding. In early summer (May and June), about half of the mosquitoes' blood meals come from the robin, despite house sparrows (*Passer domesticus*) being common and susceptible to infection. In late summer (July to September), the robins disperse and the *Culex* shift to feeding on humans, again despite the ubiquity of house sparrows. Integrating available data into a model based on a shift in mosquito feeding preference leads to the prediction that the peak transmission of WNV to humans should occur by late July to mid-August and then decline in early October when cold weather hampers mosquito activity. Seasonal shifts in mosquito feeding behavior occur across the United States and appear to intensify epidemics of several avian zoonotic viruses, not only WNV but also Western equine encephalitis virus, St. Louis encephalitis virus, and possibly other vector-borne pathogens. — CA

PLoS Biol. 4, e82 (2006).

GEOPHYSICS

A Collapsing Umbrella

Observations of volcanic plumes have provided fundamental insight into volcanic processes, one notable instance being Pliny the Younger's descriptions of Vesuvius in 79 AD. Large eruptions, like nuclear explosions, often form an umbrella-shaped plume. The top of the umbrella forms when hot gases and particles in a central eruption column reach neutral buoyancy and mix with cold dense air that is being driven upward; this process helps to stabilize the umbrella, allowing ash to fall gradually. Most such plumes have a cauliflower-shaped outer surface.

Chakraborty *et al.* describe a more ordered umbrella that formed during the November 2002 eruption of Reventador in Ecuador. In this instance, the edge of the umbrella formed large regular undulations approximately every 0.7 km, producing a shape similar to the edge of a scallop. The authors ascribe this phenomenon to an instability that occurs when the outer rim of the umbrella becomes too dense to be neutrally buoyant, a plausible result of this relatively cool eruption. Such a loss of buoyancy could lead to collapse of the umbrella, which would produce another type of volcanic flow. — BH

Geophys. Res. Lett. 33, L05313 (2006).

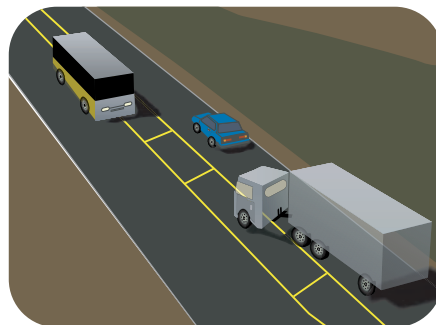
PSYCHOLOGY

Misjudging Priors

Mental models or simulations of future outcomes can be extremely helpful in planning and guiding our behavior, as when a forward model of a

reaching movement is used to reduce the variance in the trajectory of the arm. In situations where several outcomes with associated likelihoods exist, there is a known tendency, referred to as hindsight bias, for the actual outcome to inflate our post-outcome estimates of the initial likelihoods.

One arena where this bias comes into play is in the forensic reconstructions of traffic accidents, and Roeser *et al.* have examined whether using computerized simulations (versus text and diagram visual aids) elicits these overestimates. They find that animated sequences exacerbate hindsight bias and, more intriguingly, that the bias reverses when the post-outcome estimate is compared to one made just before the time of collision. This so-called propensity effect



An accident about to happen . . . or not?

describes our sense that the collision is destined to occur before it takes place, something we are surprisingly less certain about after the collision has actually occurred. — GJC

Psychol. Sci. 17, 305 (2006).

CHEMISTRY

Small-Scale Synergy

In metallic and semiconductor nanoparticles, the material properties can be tuned simply by changing the particle size. Shi *et al.* have explored the additional dimension of varying nanoparticle composition to incorporate multiple kinds of materials—specifically magnetic-metallic, magnetic-semiconducting, and semiconducting-metallic hybrids, as well as ternary combinations.

The synthetic strategy involved spontaneous epitaxial nucleation and growth of the second and third components onto seed particles in high-temperature organic solutions. For the magnetic-metallic particles (Fe_3O_4 grown on gold), solvent choice influenced the particle morphology, with good electron donors leading to core-shell geometries and poor electron donors yielding peanut-shaped fused particles. For Au-PbS particles, which combine a metal and a semiconductor, the choice of solvent did not influence the particle morphology, but the concentration of gold seed particles was critical. Finally, heating strategy and seed particle dimensions were the key variables for setting the ternary particle morphologies. The optical and magnetic properties of the particles were influenced by the hybrid interface. For example, the Au plasmon resonances were red-shifted in the hybrid particles; at the same time, the magnetization saturation field of the Fe_3O_4 -Au particles was an order of magnitude greater than that of pure magnetite. — MSL

Nano Lett. 6, 10.1021/nl0600833 (2006).

Continued on page 1677

Continued from page 1675

CHEMISTRY

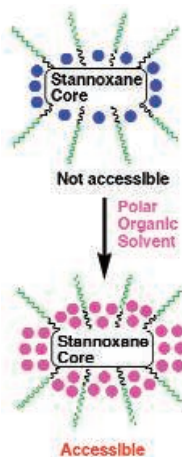
Switching Philicity

The immiscibility of organic and aqueous solutions (such as oil and vinegar) underlies a wide range of practical chemical separations. For versatility, liquid fluorocarbons have come into increasing use over the past decade as a third solvent phase, into which highly fluorinated solutes

partition from both water and the more traditional organic solvents.

Orita *et al.* were therefore surprised to find that a hydrated distannoxane complex bearing linear fluorocarbon tails—an Sn-O-Sn core with two $C_6F_{13}C_2H_4$ chains and a perfluorooctane sulfonate chain appended to each

Displacement of water (blue) by ethyl acetate (pink) induces fluorphilicity.



Sn—failed to dissolve in common fluoruous solvents such as FC-72. The compound did dissolve in polar organic liquids (ethyl acetate, acetone, and tetrahydrofuran), and subsequently partitioned into the fluoruous phase upon addition of FC-72 to the solution. The authors explain these observations by suggesting that the waters of hydration initially bound to the tin repel the fluoruous solvent but can be displaced by polar organics, which in turn allows the fluoruous liquid to approach. The compound proved useful as a

homogenizing agent for fluoruous and organic solvents, with 1.7 g nearly tripling the solubility of ethyl acetate in FC-72. — JSY

J. Am. Chem. Soc. **128**, 10.1021/ja058105v (2006).

DEVELOPMENT

More Is Bigger

Multicellular organisms can grow by making more cells or by making larger ones. The nematode *Caenorhabditis elegans* uses both methods: Cell proliferation drives worm growth until sexual maturity, whereas cell growth (mainly of epidermal cells) accounts for the twofold increase in size during adulthood. Growing adult cells also undergo endoreduplication, wherein genomic DNA is replicated repeatedly without cell division, resulting in each cell containing multiple copies of the genome (polyploidy) rather than just two.

Lozano *et al.* address the question of whether endoreduplication is directly responsible for adult growth in the worm. Blocking endoreduplication after the final larval molt results in dwarf worms that are roughly half the size of wild-type adults, whereas in a tetraploid strain, adult worms are roughly 40% larger than normal.

Cyclin E is involved in the control of endoreduplication in a number of organisms, including *C. elegans*, and adult worms mutant for *cye-1* have both reduced epidermal ploidy and are dwarfed, often to less than half the size of comparable wild-type adults. Although it is clear that endoreduplication can account for the growth of polyploid somatic cells in worms, cells that remain diploid in the adult are presumably stimulated to grow by their polyploid neighbors. — GR

Curr. Biol. **16**, 493 (2006).



www.stke.org

<< Larger Pipe, Lower Resistance

The pathogenesis of hypertension—a risk factor for heart disease, kidney disease, and stroke—is complex and poorly understood. Zacchigna *et al.* find that mice lacking elastin microfibril interface-located protein 1 (Emilin1), a secreted extracellular matrix protein expressed in the cardiovascular system, had high blood pressure in conjunction with decreased blood vessel diameter and increased peripheral resistance. Emilin1 contains a cysteine-rich domain, as do other proteins involved in the regulation of growth factor signaling, leading the authors to investigate the relationship between Emilin1 and transforming growth factor- β (TGF- β), which plays a critical role in vascular development and pathophysiology. Emilin1 blocked TGF- β signaling upstream of receptor activation and did not interfere with ligand/receptor binding or signaling in response to mature TGF- β 1. Rather, Emilin1 bound to proTGF- β 1, preventing its proteolytic processing and the production of biologically active TGF- β 1. TGF- β signaling was enhanced in the aortic wall of the mice lacking Emilin1, and inactivation of one *TGF- β 1* allele in *Emilin1* knockout mice restored normal blood vessel diameter and blood pressure. Thus, the authors conclude that Emilin1 acts to regulate blood pressure by modulating TGF- β processing and thus the availability of the biologically active form. — EMA

Cell **124**, 929 (2006).